Time reversal through a solid-liquid interface and super-resolution

Chrysoula Tsogka* George C. Papanicolaou†

December 15, 2002

Abstract

We present numerical computations that reproduce the time reversal experiments of Draeger, Cassereau and Fink (Draeger et al., 1998), where ultrasound elastic waves are time reversed back to their source with a Time Reversal Mirror (TRM) in a fluid adjacent to the solid. We also show numerically that multipathing caused by random inhomogeneities improves the focusing of the back-propagated elastic waves beyond the diffraction limit seen previously in acoustic wave propagation (Dowling and Jackson, 1990; Dowling and Jackson, 1992; Fink, 1999; Kuperman et al., 1997; Derode et al., 1995), which is called super-resolution. A theoretical explanation of the robustness of super-resolution along with several numerical computations that support this explanation is in (Blomgren et al., 2002). Time reversal with super-resolution can be used in non-destructive testing and, in a different way, in imaging with active arrays (Borcea et al., 2002).

PACS numbers: 43.60.Tj, 43.60.Cg, 43.60.Rw

1 Introduction

Time-reversal invariance of wave equations can be used to refocus optimally a signal back onto the source that emitted it. The way to do this is as follows. A time reversal mirror (TRM), which is an array of transducers (receivers and transmitters), is used to record the wave as a function of time and then, in a second step, the recorded field is time reversed and re-transmitted. The time reversed wave back-propagates through the medium and refocuses on the initial source position. This refocusing property has several applications in medicine, geophysics, non-destructive testing, etc (Fink, 1999).

From the experimental point of view, time-reversal devices are designed to work with ultrasound, primarily in a fluid environment. In (Draeger et al., 1998) the results of a physical experiment were reported, showing that time reversal refocusing can be realized also in solids. The solid is surrounded by a fluid in which the TRM device is located. Following the experimental setting in (Draeger et al., 1998) we consider here the problem described in Figure 1.

A point source located in the solid is used to emit the initial wave U_I. The initial pulse can be either a pressure (longitudinal) or a shear (transverse) wave, or both. The emitted wave propagates in the solid and is partially transmitted into the fluid (water), where both types of waves (P and S) are converted to pressure

*INRIA-Rocquencourt, France and CNRS/LMA, 31 Chemin Joseph Aiguier, 13402 Marseille cedex 20, FRANCE, tsogka@lma.cnrs-mrs.fr. This work was done while visiting the Department of Mathematics at Stanford University.

†Department of Mathematics, Stanford University, Stanford CA 94305; papanico@math.stanford.edu. Work supported by grants AFOSR F49620-98-1-0211 and NSF-DMS-9971972

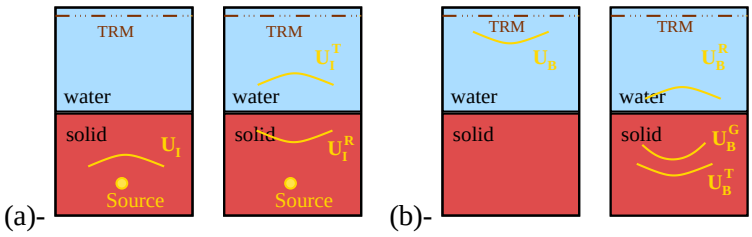

Figure 1: Description of the problem : (a) a point source emits an initial wave in the solid, the wave is partially transmitted into the fluid and recorded by the TRM device. (b) The time-reversed field is re-emitted by the TRM, the wave back-propagates in the fluid and generates two wavefronts in the solid.

waves (U_I^T). After propagation in the fluid the transmitted waves are recorded by a TRM device (located in the fluid). For each initial type of wave (P or S) there are also two reflected wavefronts (P and S), denoted U_I^R, which propagate in the opposite direction in the solid and thus cannot be captured by the TRM device.

In the second step the time-reversed field is re-emitted into the fluid using the TRM device. The pressure wave U_B back-propagates in the fluid and generates two transmitted wavefronts in the solid. This is because the back-transmission of a pressure wavefront through the fluid-solid interface generates both a pressure and a shear wave "back-propagating" in the solid. However, only one of these two wavefronts corresponds to the "initial, physical" wave, the one denoted U_B^T. The second transmitted wave U_B^G is a "ghost" wave and is unwanted. However, we will see that in the examples that we consider here these ghost waves do not degrade the time reversal focusing because they are rather diffuse and they have different arrival times relative to the physical waves. In general, interference of ghost waves with physical waves will depend on the distance of the source from the interface, the pressure and shear wave velocities and the pulse width. In (Draeger et al., 1997) a theoretical and numerical formulation was presented, describing the time reversal process through a fluid-solid interface. The theory is based on the compressional and shear potentials formulation for elastodynamics and uses Fourier transforms in the transverse directions (x, y). Although this formulation describes the phenomena in the case of simple media (i.e., for which the (x, y)-Fourier transform of the potential exists), it cannot be used in a more complex setting such as for heterogeneous, random media.

Time-reversal refocusing through heterogeneous media is very interesting because multipathing gives rise to super-resolution. This means that the refocusing onto the source is tighter than the diffraction limit and is, moreover, statistically stable. Super-resolution has been observed and analyzed before in acoustics (Dowling and Jackson, 1990; Dowling and Jackson, 1992; Fink, 1999; Kuperman et al., 1997; Derode et al., 1995). The phenomenon of statistical stability in super-resolution was explained theoretically and confirmed by numerical simulations in (Blomgren et al., 2002). Statistical stability here means that the refocused field is self-averaging in the time domain and does not depend on the particular realization of the random medium.

In this work we carry out a systematic analysis of the refocusing resolution obtained by time-reversal through a fluid-solid interface. We first consider a generalization of the usual expression for the resolution limit in the homogeneous case and then validate it numerically. We next consider randomly inhomogeneous media and show that statistically stable super-resolution occurs. The full theory for super-resolution of elastic waves is a complex project that involves the radiative transport theory of elastic waves (Ryzhik et al., 1996) and will be presented elsewhere.

In our numerical simulations we solve the partial differential equations directly in the time domain. This allows us to better illustrate the physical phenomena since time-reversal is a time-domain phenomenon.

2 The time reversal problem

Our aim is to reproduce numerically the experiment described by Figure 1, in several different situations. The general characteristics of the problem are based on the physical experiments in (Draeger et al., 1998),(Draeger et al., 1997), described in Figure 2.

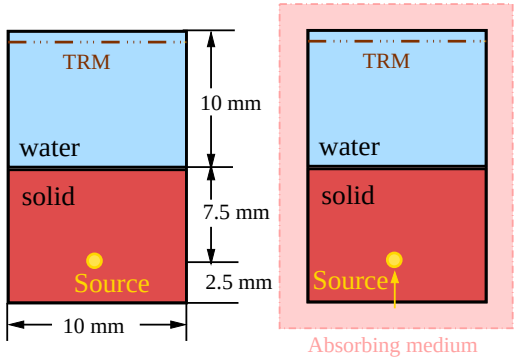

Figure 2: The computational setup. The dimensions of the problem are shown in the figure on the left and are taken from the physical experiment described in (Draeger et al., 1998). The medium is considered to be infinite in all directions and thus in the numerical computations an absorbing layer surrounds the domain, shown on the right.

For wave propagation in the solid we use the mixed velocity stress formulation of elastodynamics, given by

$$\begin{aligned} \varrho\, \partial_t v - \mathbf{div}\sigma &= f \quad \text{in } \mathbb{R}^2 \times]0,T[\\ A\, \partial_t \sigma - \varepsilon(v) &= 0 \quad \text{in } \mathbb{R}^2 \times]0,T[, \end{aligned} \tag{2.1}$$

together with the initial conditions

$$v(t=0) = 0 \; ; \; \sigma(t=0) = 0 \text{ in } \mathbb{R}^2. \tag{2.2}$$

In (2.1) the unknowns are, σ the stress tensor and v the velocity which is the time derivative of the displacement u, i.e., $v = \partial_t u$. The elastic medium is characterized by the density ϱ and the compliance matrix A. We assume that the geometry of the problem is invariant in the y-direction, i.e, the one perpendicular to the (x, z) plane of the paper. The support of the source is a line in the y direction, radiating a cylindrical P-SV displacement pulse such that only the P-SV component of this field is non-vanishing and invariant with respect to y. Consequently, for isotropic solids the total field is P-SV-polarized and invariant with respect to y, i.e., the problem is two-dimensional, with the displacement field depending only on (x, z) and on time t. In this case, $C(\mathrm{x})$, the matrix of elastic moduli reduces to a 4×4, positive definite matrix and A is defined by,

$$A = A(\mathrm{x}) = C^{-1}(\mathrm{x}) \; .$$

We denote by $\varepsilon(u)$ the linearized strain tensor

$$\varepsilon_{ij}(u) = \frac{1}{2} \left(\partial_j u_i + \partial_i u_j \right) \; .$$

The stress tensor is related to the strain tensor by the generalized Hooke's law

$$\sigma = \sigma(u)(\mathrm{x}, t) = C(\mathrm{x}) \varepsilon(u)(\mathrm{x}, t) \; .$$

In the fluid we solve the same system of equations (2.1), (2.2) by considering it as a solid with zero shear velocity (we take the Lamé coefficient μ equal to zero). In that case, system (2.1) can also be written in the following form,

$$\begin{aligned} \varrho_w \, \partial_t v - \nabla p &= f \ , \\ \frac{1}{\lambda} \partial_t p - \mathbf{div} v &= 0 \ , \end{aligned} \tag{2.3}$$

where

$$p = \sigma_{xx} = \sigma_{zz} \ ; \ \sigma_{xz} = 0.$$

Thus, to simulate the forward problem (see Figure 1-a) we solve system (2.1), (2.2), which is an elastic medium composed of two layers : the upper one, with zero shear velocity is the fluid and the lower one is the solid. The ultrasonic pulse (initial wave) is created by a point load source of the form

$$f(\mathrm{x}, t) = F_1(t) \vec{g}(r) \ , \tag{2.4}$$

with

$$\left| \begin{array}{l} F_1(t) = \left\{ \begin{array}{ll} e^{-\pi^2 f_0^2 (t-t_0)^2} & \text{if } t \leq 2t_0 \\ 0 & \text{if } t > 2t_0 \end{array} \right. , \\ t_0 = \dfrac{1}{f_0}, \ f_0 \text{ the central frequency,} \end{array} \right. \tag{2.5}$$

Here $\vec{g}(r)$ is the radial function

$$\vec{g}(r) = \left(1 - \frac{r^2}{r_s^2} \right)^3 \ 1_{B_s} \vec{d} \tag{2.6}$$

with 1_{B_s} the characteristic function of the disc B_s, centered at S with radius r_s. The coordinates of the source point S are (x_s, z_s). The function $\vec{g}(r)$ is a smooth approximation of the delta function at S. The radius r_s is small, typically a few discretization steps. The vector $\vec{d}$ gives the direction of the initial pulse. We take

$$\vec{d} = (0, 1) \ ,$$

which is a z-directional source that creates both a pressure and a shear initial wave. This source function is a z-directional force applied at S (see Figure 2). We are interested in the ultrasonic regime so we take $f_0 = 3.5 MHz$ as the central frequency of the source. In Figure 3 we plot $F_1(t)$ as a function of time.

To simulate the backward problem we solve the system

$$\begin{aligned} \varrho \, \partial_t v^b - \mathbf{div} \sigma^b &= 0 && \text{in } (\mathbb{R}^2 - \Gamma) \times]0, T[\\ A \, \partial_t \sigma^b - \varepsilon(v^b) &= 0 && \text{in } (\mathbb{R}^2 - \Gamma) \times]0, T[, \\ \sigma^b_{zz}(x, z_r, t) &= \sigma_{zz}(x, z_r, T - t) && \text{on } \Gamma \times]0, T[, \end{aligned} \tag{2.7}$$

together with the initial conditions

$$v^b(t = 0) = 0 \ ; \ \sigma^b(t = 0) = 0 \text{ in } \mathbb{R}^2, \tag{2.8}$$

where Γ is the line

$$\Gamma = \{(x, z), x \in [x_1, x_2], z = z_r\},$$

representing the TRM device, i.e., the line of the transducers at which the solution of the forward problem ($\sigma_{zz}(x, z_r, T - t)$) is recorded and then re-transmitted while solving the backward problem.

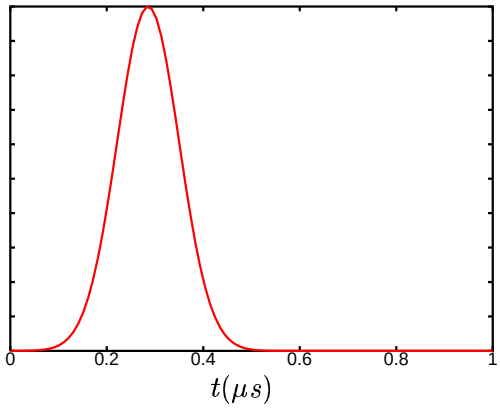

Figure 3: The source function $F_1(t)$ as a function of time. The maximum occurs at time $t_0 = 1/f_0 = 0.286\mu s$

In both cases, that is, for the forward and the backward simulation, we assume that the problem is posed in the whole space. To solve it numerically, we surround the domain with an absorbing layer. More precisely, we couple system (2.1)-(2.2) (or (2.7)-(2.8)) with the perfectly matched absorbing layer model (PML) for elastodynamics. This is a very efficient absorbing layer model, introduced by Berenger (Bérenger, 1994) for Maxwell's equations and generalized to elastodynamics in (Collino and Tsogka, 2001).

In what follows the fluid is water, characterized by the sound speed $V_w = 1500m/s$ and the density $\varrho_w = 1000kg/m^3$. The sound speed is given by

$$V_w = \sqrt{\frac{\lambda}{\varrho_w}},$$

with λ the Lamé bulk modulus. The elastic solid is an aluminum alloy which is homogeneous and isotropic. It is characterized by the propagation speeds $V_p = 6300m/s$ (pressure), $V_s = 3150m/s$ (shear) and the density $\varrho = 2700kg/m^3$. We recall that,

$$V_p = \sqrt{\frac{\lambda + 2\mu}{\varrho}} \; ; \; V_s = \sqrt{\frac{\mu}{\varrho}},$$

where μ is the Lamé shear modulus.

2.1 The computational setup

The numerical method we use is based on the discretization of the mixed velocity stress formulation for elastodynamics (i.e., system (2.1)-(2.2)). For the space discretization we use a new finite element method (see (Bécache et al., pear; Bécache et al., 1997)), which is compatible with mass-lumping techniques (i.e., it leads to explicit time discretization schemes) and for the time discretization we use a centered 2nd order finite difference scheme.

The computational domain, which is a rectangle, is descretized with a finite element mesh composed of $N_x \times N_z$ square elements of size h. The numerical scheme we use is stable subject to a CFL condition of the type

$$\Delta t \leq C \; h,$$

where the constant C is known explicitly ($C = 1/V_p$) and depends on the maximum wave speed in the computations.

As remarked already, we model the fluid as a solid with zero shear wave speed. For numerical stability, however, we take a non-zero but very small shear wave speed. For example, for water we take $V_p = V_w = 1500m/s$ and $V_s = 1m/s$.

3 Reflection-transmission at the liquid-solid interface

We consider here the problem described in Figure 2. The computational domain is composed of $N_x \times N_z = 330 \times 660$ elements of size $h = 0.03mm$ which corresponds to 30 points per shear wavelength or equivalently to 15 points per wavelength in the water. The different wavelengths involved are $\lambda_w = 0.43mm$ in the water, $\lambda_s = 0.9mm$ for the shear wave in the solid and $\lambda_p = 1.8mm$ for the pressure wave in the solid. The total duration of the experiment is $T = 9.5\mu s$, which corresponds to 1995 time steps.

We consider here the z-directional source given by equations (2.4), (2.5) and (2.6). As already noted, this source generates both a pressure and a shear wave. In Figures 4 - 5 we present the first part of the computations, which is the forward problem. The waves emitted from the source propagate in the solid, are partially transmitted and reflected at the fluid-solid interface, and are recorded by the TRM device in the fluid. Snapshots of the solution (the norm of the velocity field) are presented at different times.

We use the following notation for the different wavefronts that are generated. The initial waves emitted from the source are denoted by P (pressure) and S (shear). For the transmitted (respectively reflected) wavefronts we use two letters : the first one indicates the type of the incident wave before transmission (resp. reflection) and the second one the type of the transmitted (resp. reflected) wave. For example, the reflected shear wave induced from a pressure wave at the fluid-solid interface is a P-S reflected wave.

In Figures 6 - 7 we show the second part of the computation, the backward problem. The time-reversed field is re-emitted in the fluid using the TRM device. We have two pressure waves, the S-P and P-P transmitted back-propagating in the fluid. Note that the S-P wave, which arrived last, propagates now first. Upon arrival at the interface, each of the two waves generates three waves: one reflected and two transmitted. However, only one of the transmitted waves corresponds to the physical wave, the one initially emitted from the source. The other one is a ghost wave. For this computation there are two physical back-transmitted waves in the solid, (P-P-P and S-P-S), and two ghost waves, (P-P-S and S-P-P). As shown in Figure 8 the two physical waves focus at the same time on the original source position, while the two ghost waves are not focused, arrive near the source at different times and their amplitude is weaker. Note also that the focal spot has approximately the size of the biggest wavelength, which is the pressure wavelength $\lambda_p = 1.8mm$.

4 Refocusing Resolution in a homogeneous medium

The refocusing property of the TRM device is important in many applications, in medicine, geophysics, non-destructive testing, etc., so we need to understand both theoretically and computationally the resolution limits of the refocused signal.

We first consider homogeneous media and recall some basic facts about resolution limits in time-reversal acoustics.

In an homogeneous medium the cross-range spatial resolution of acoustic (scalar) waves may be estimated by (see (Blomgren et al., 2002))

$$d = \frac{\lambda L}{\alpha} \tag{4.9}$$

where λ is the wavelength, L the distance between the source and the TRM device and α the aperture of the

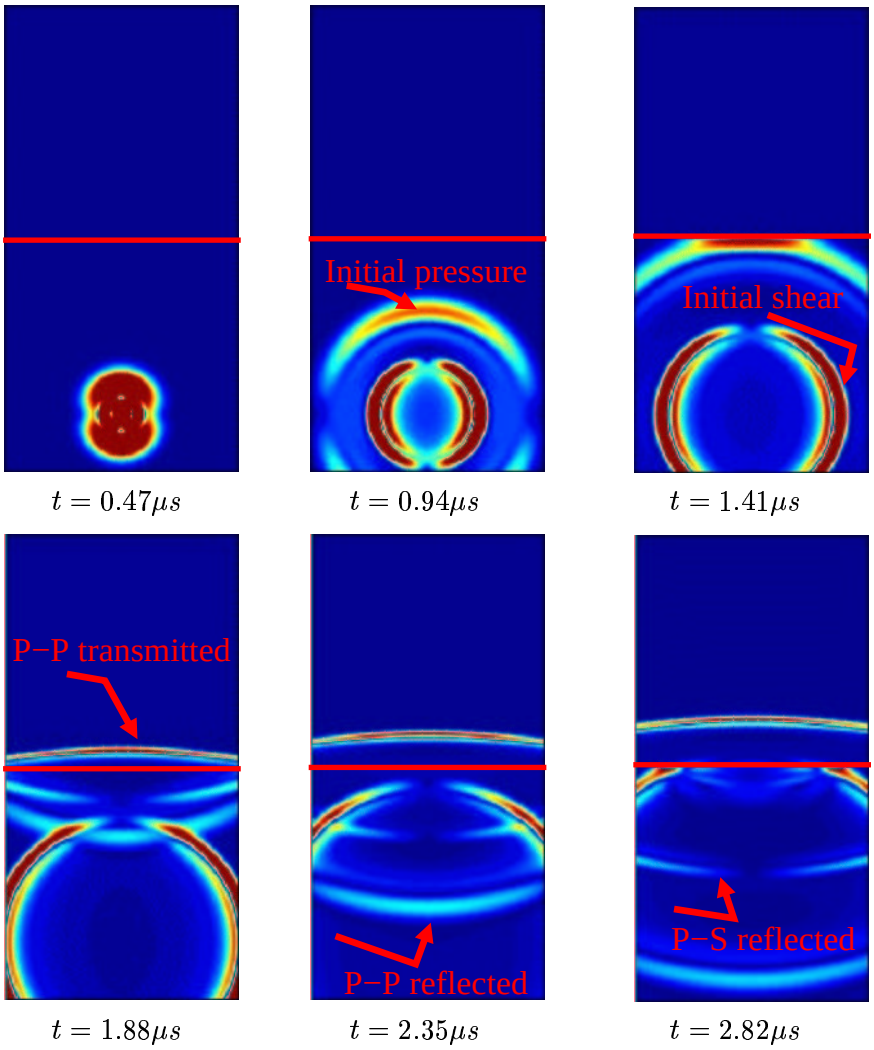

Figure 4: The forward problem : snapshots of the norm of the velocity field at different times. The source emits both a pressure and a shear wave which propagate in the solid. Since the pressure wave velocity is bigger, the pressure wave arrives first at the fluid-solid interface where it generates 3 wavefronts : a pressure wave (P-P), transmitted in the fluid, and two reflected waves, a pressure (P-P) and a shear wave (P-S).

mirror. This estimate is valid provided that $\alpha \ll L$. We can generalize this to the case of time reversal via a fluid-solid interface as shown in Figure 9.

The distance between the source and the mirror L, is now divided in two parts

$$L = L_s + L_w$$

where L_s is the distance in the solid and L_w the one in the water. The distance traveled, in wavelengths, divided by the width of the TRM is a natural generalization of the cross-range spatial resolution

$$d = \frac{\lambda_p L_s + \lambda_w L_w}{\alpha}, \tag{4.10}$$

with λ_p the wavelength of the pressure wave in the solid, and λ_w the wavelength in the water.

In what follows we present several numerical results which confirm the validity of this relation.

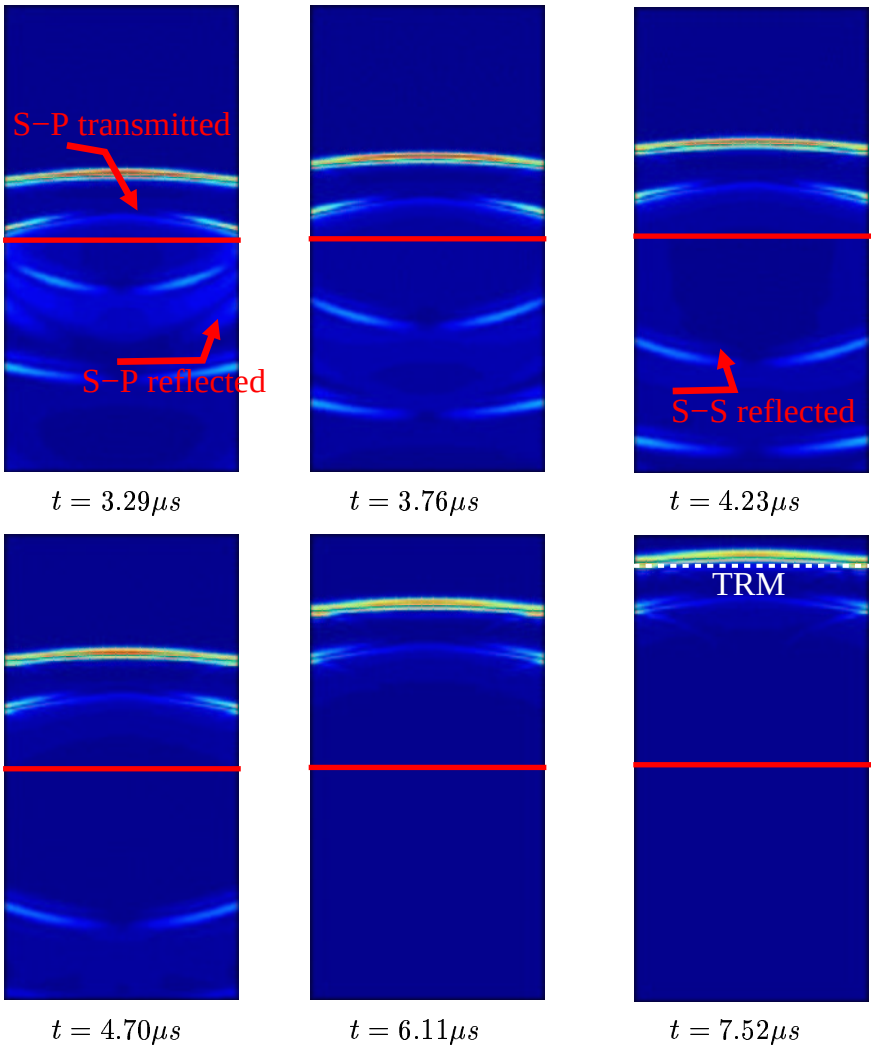

Figure 5: The forward problem : snapshots of the norm of the velocity field at different times. Following the pressure wave, the shear wave arrives at the interface. It generates three wavefronts, in exactly the same manner as the pressure wave : an S-P transmitted , an S-P reflected and an S-S reflected wave.

4.1 Numerical estimation of the resolution limit

The setup of the problem is shown in Figure 9 and all the physical parameters are the same as in the previous computations (see also Figure 2).

The ultrasonic pulse is created by the same source as before (cf. equations (2.4), (2.6)) but now has a Ricker form in time, that is, the function $F_1(t)$ in (2.4) is replaced by $F_2(t)$,

$$F_2(t) = \begin{cases} -2\pi^2 f_0^2 (1 - 2\pi^2 f_0^2 (t - t_0)^2) e^{-\pi^2 f_0^2 (t-t_0)^2} & \text{if } t \leq 2t_0 \\ 0 & \text{if } t > 2t_0 \end{cases}, \tag{4.11}$$

We use the source function $F_2(t)$ because we can measure the resolution at the initial source position easier, as this pulse has only one maximum. In Figure 10 we plot $F_2(t)$ as a function of time. The maximum

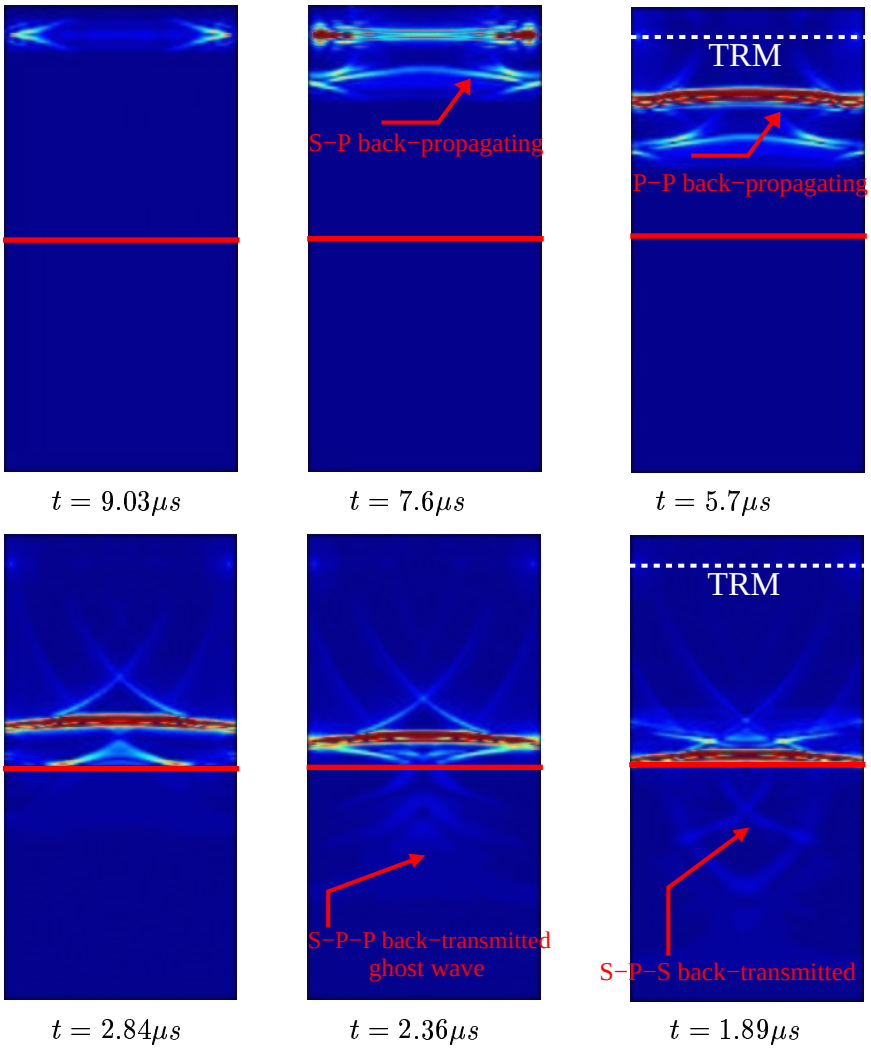

Figure 6: The backward problem : snapshots of the norm of the velocity field at different times. The two pressure waves (S-P and P-P) recorded by the TRM are time-reversed and re-emitted in the fluid. Note that the S-P wave, which arrived last, propagates now first and thus arrives first at the fluid-solid interface where it generates three waves: one reflected and two transmitted (S-P-P and S-P-S). Only the S-P-S is a physical wave and corresponds to the initial shear wave emitted from the source. The S-P-P wave is a ghost wave. As its velocity is bigger it arrives first at the source location and is already outside the computational domain when the two physical waves focus on the source (see Figure 8).

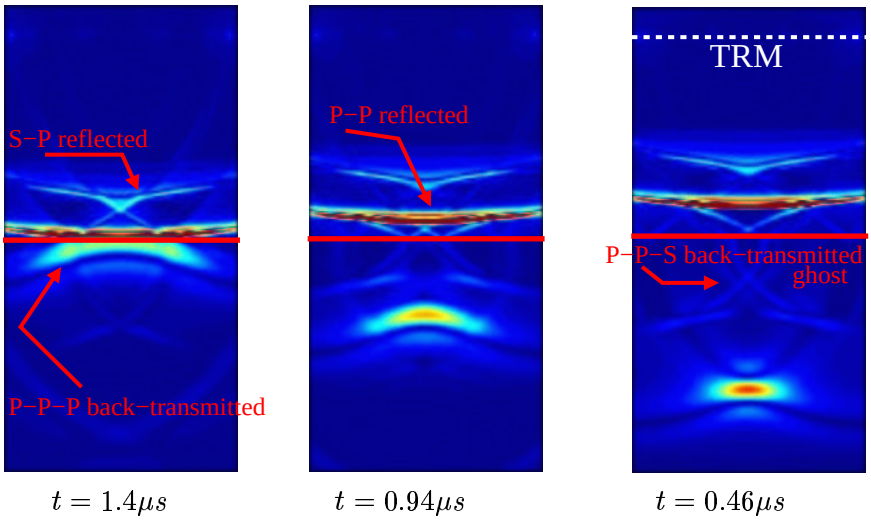

Figure 7: The backward problem : snapshots of the norm of the velocity field at different times. The pressure wave P-P arrives second at the fluid-solid interface where it generates a reflected pressure wave (P-P), the physical P-P-P back-transmitted wave, and the ghost P-P-S back-transmitted wave. This ghost wave has a smaller velocity and thus remains behind the source location when the two physical waves focus on it (see Figure 8).

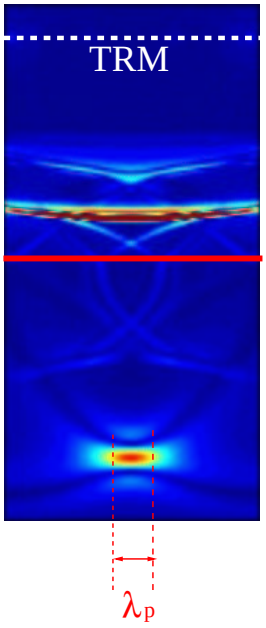

Figure 8: The backward problem : snapshot of the norm of the velocity field at time $t = t_0 = 0.286\mu s$, the time when the maximum in the emitted pulse occurred. This is also the time at which the two physical waves are expected to refocus onto the source location. For this setup, the size of the focal spot is approximately equal to the size of the biggest wavelength $\lambda_p = 1.8mm$.

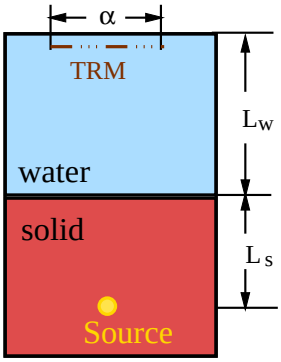

Figure 9: Setup of the computational problem. Here L_s is the distance between the source and the fluid-solid interface and L_w the one between the fluid-solid interface and the TRM device. The width of the TRM device is denoted by α.

amplitude (in absolute value) for this function occurs at time $t = t_0 = 0.286\mu s$ (the same as for $F_1(t)$). This is the time at which the two physical waves are expected to refocus onto the source location.

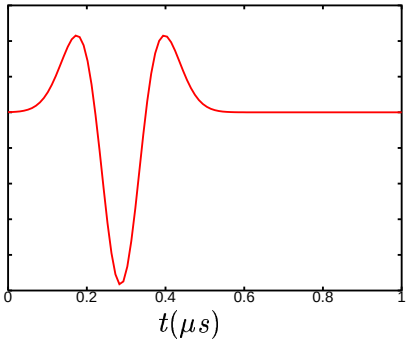

Figure 10: The source function $F_2(t)$ as a function of time.

In the numerical computations we use a finite element mesh composed of $N_x \times N_z (= 500 \times 1000)$ square elements. The space discretization step is $h = 0.02mm$.

We present here several numerical results which confirm relation (4.10). We systematically change the parameters λ_p, λ_w, L_p, L_s and α and compare the refocusing resolution obtained numerically d_{num} with the one given by relation (4.10).

We vary first the aperture of the TRM mirror. Snapshots of the back-propagated field are presented in Figure 11 for $\alpha = 9.42mm$, $8.5mm$, $7.54mm$, $6.62mm$, $5.66mm$ and $4.74mm$,that is, we begin with a mirror of size $\alpha = 9.42mm$ and then we systematically reduce the size by 10%. As expected the refocused spot size increases when the aperture of the mirror decreases. To see the results more quantitatively we present in Figure 12 the norm of the back-propagated field at $z = z_s$ (the level of the source position).

In Table 1 we compare d_{num}, the refocusing resolution obtained numerically, with the theoretical one given by (4.10). We compute d_{num} with a least squares fit of the curvature of the refocused field (in the cross-range direction) at the source location (see Figure 12 on the right).

In the second set of computations we vary the frequency of the emitted signal. More precisely we take $f_0 = 3.5MHz$, $3.15MHz$, $2.81MHz$ and $2.4MHz$. This changes the wavelengths λ_p and λ_w , making

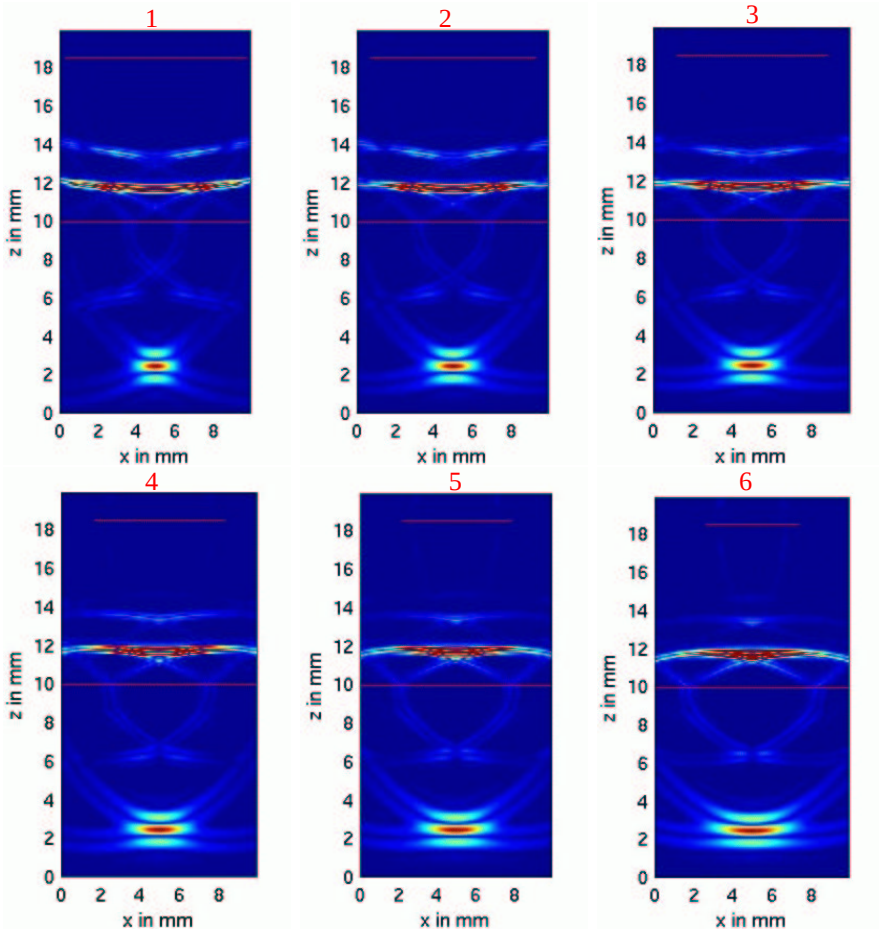

Figure 11: Normalized snapshots of the norm of the velocity field at time $t = t_0 = 0.286\mu s$. The aperture of the TRM varies from $9.42mm$ to $4.74mm$ in the snapshots 1 to 6.

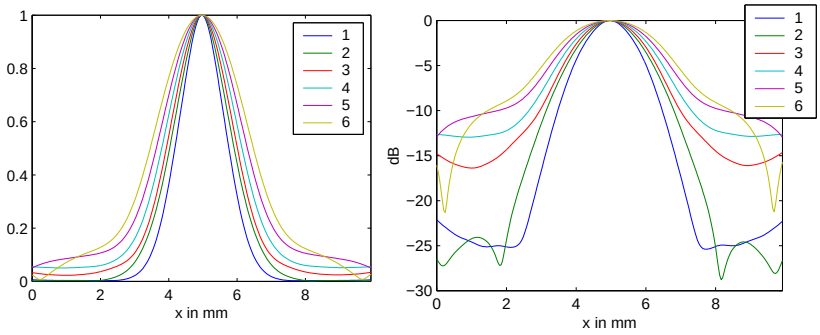

Figure 12: The norm of the back-propagated field at the source level : normalized scale on the left and in dB on the right. The six curves in each figure correspond to different apertures of the TRM (from $9.42mm$ to $4.74mm$).

α in mm	d in mm	d_{num} in mm	error %
9.42	1.82	1.75	3.75
8.5	2.01	2.07	2.67
7.54	2.27	2.41	6.17
6.62	2.59	2.82	8.92
5.66	3.02	3.29	8.88
4.74	3.61	3.89	7.70

Table 1: Comparison between the theoretical (d) and the numerical (d_{num}) estimate of the refocusing resolution for different apertures of the TRM device.

them longer as frequency decreases.

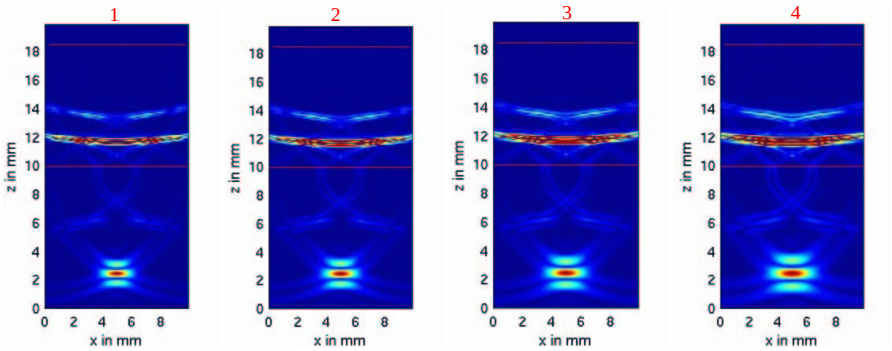

Figure 13: Normalized snapshots of the norm of the velocity. The frequency of the signal varies from $3.5MHz$ to $2.4MHz$ in the snapshots 1 to 4.

In Figure 13 we present snapshots of the back-propagated field for the different values of f_0. The same results at the source level are shown in Figure 14.

The theoretical and the numerical values of the refocusing resolution for these different frequency values are given in Table 2. When frequency decreases, the refocused spot size increases as it is proportional to the wavelengths.

We finally present a set of numerical computations in which the propagation distances L_p and L_w vary. In the first four computations the distance between the source and the mirror is fixed but we change the fluid-solid interface position (L_p increases and L_w decreases). In the last two computations the total distance L increases. Field amplitudes at the level of the source location are shown in Figure 15.

5 Refocusing resolution and stability in a random medium

In this section we present numerical results for time-reversal through random media. The random heterogeneities are in the fluid only (see Figure 16). We assume that the sound speed in the liquid fluctuates randomly about a uniform value and that the fluctuations are weak, that is, their standard deviation varies

f_0 in MHz	λ_p in mm	λ_w in mm	d in mm	d_{num} in mm	error %
3.5	1.8	0.43	1.82	1.75	3.75
3.15	2.0	0.48	2.02	1.95	3.49
2.81	2.24	0.54	2.26	2.20	2.51
2.4	2.56	0.61	2.58	2.54	1.66

Table 2: Comparison between the theoretical (d) and the numerical (d_{num}) estimate of the refocusing resolution for different values of f_0.

L_p in mm	L_w in mm	$L = L_p + L_s$ in mm	d in mm	d_{num} in mm	error %
7.48	8.52	16.0	1.82	1.75	3.75
8.28	7.72	16.0	1.93	1.92	0.94
9.32	6.68	16.0	2.08	2.14	2.51
10.66	5.34	16.0	2.28	2.42	6.07
8.48	8.52	17.0	2.01	1.96	2.15
9.48	8.52	18.0	2.20	2.20	0.10

Table 3: Comparison between the theoretical (d) and the numerical (d_{num}) estimate of the refocusing resolution for different values of L_p and L_w.

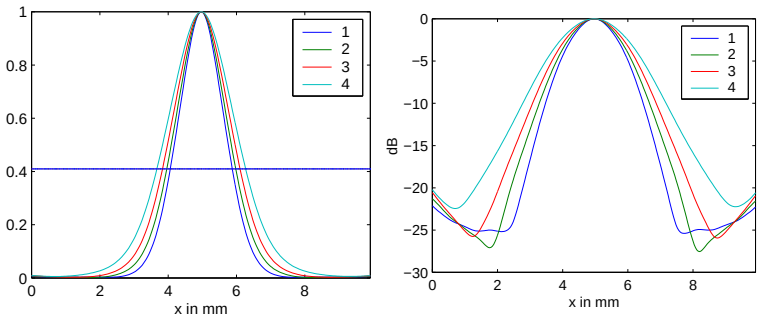

Figure 14: The norm of the back-propagated field at the source level : normalized scale on the left and in dB on the right. The four curves in each figure correspond to different wavelengths λ_p, λ_w (see Table 2 for the values).

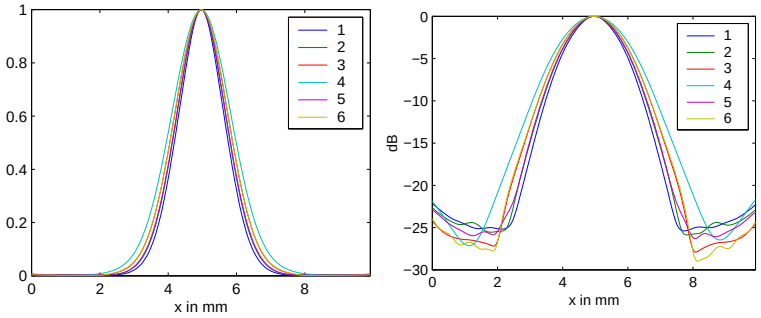

Figure 15: The norm of the back-propagated field at the source level : normalized scale on the left and in dB on the right. Six different curves are drawn in each figure and they correspond to different values of L_w and L_p (see Table 3).

from 1% to 10%, while their correlation length is comparable to the wavelength. This is a regime where multipathing is significant even when the standard deviation of sound speed fluctuations is only a few percent, and in which the statistical stability and super-resolution properties of time reversal can be observed (Papanicolaou et al., 2002a).

In the numerical simulations, we use statistically homogeneous Gaussian random velocity fields, with constant mean $c_0 = 1.5$km/s, correlation length $C_l = 0.3$mm, 0.5mm and standard deviation s ranging from 1% to 10%. The random fluctuations of the sound speed are generated numerically with Fourier series having suitably calibrated Gaussian, complex valued, random amplitudes. The spatial correlation function is an isotropic exponentiali, approximately, with decay constant equal to the reciprocal of the correlation length.

The aperture of the TRM device is chosen small enough ($\alpha = 4.74mm$) in order to be able to observe super-resolution phenomena. All the other dimensions of the problem are the same as before (see Figure 16).

We present in Figure 17 the first set of computations. The snapshot on the left corresponds to the homogeneous medium. For the three other snapshots we a use random media with the same correlation length but with different variance for the fluctuations. The characteristics of the different random media are given in Table 4. We also give in this table the maximum contrast for each medium. In these computations the correlation length is $0.5mm$ so it is of the same order as the wavelength in the water (i.e, $\lambda_w = 0.43mm$)

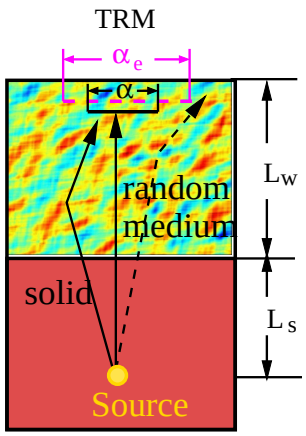

Figure 16: Setup of the computational problem: the water is replaced by a fluid with random heterogeneities. Multipathing caused by random heterogeneities makes the effective size α_e of the TRM larger than its physical size α, and thus improves the refocusing of the back-propagated elastic waves beyond the diffraction limit.

In Figure 18 we present the refocused field amplitude at the source location. In Figure 19 we show the results

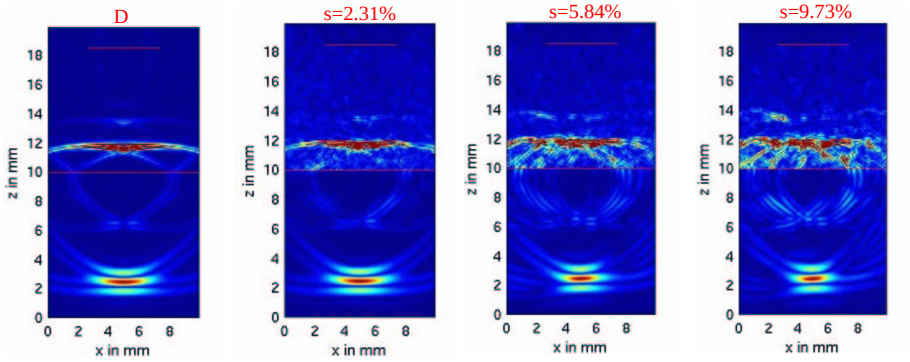

Figure 17: Normalized snapshots of the norm of the velocity. The simulation for the deterministic (homogeneous) medium is on the left and for the random media on the right. The standard deviation of the fluctuations is 0.0%, 2.31%, 5.84% and 9.73% from left to right. The correlation length is comparable to the wavelength.

of a second set of computations. The random medium has now a smaller correlation length ($C_l = 0.3mm$) Snapshots of the refocused field are presented in Figure 19 and the amplitude at the source location in Figure 20.

Multipathing or multiple scattering effects are observable and significant when the waves interact strongly with the medium inhomogeneities. That is why in the simulations we use random fluctuations with correlation length comparable to the wave length. In the regime of our numerical experiments, if the correlation length is much shorter than the wavelength then it will be averaged out and the medium will behave like a homogeneous one. If the correlation length is much longer than the wave length then the medium will again behave like a homogeneous one but with different effective properties. Various scaling limits involving the correlation length are discussed in more detail in (Papanicolaou et al., 2002a).

As we can observe from the results in Figure 18 the field is not symmetric, this is due to the particular realization of the random medium and it does not affect the super-resolution, as the asymmetry appears far

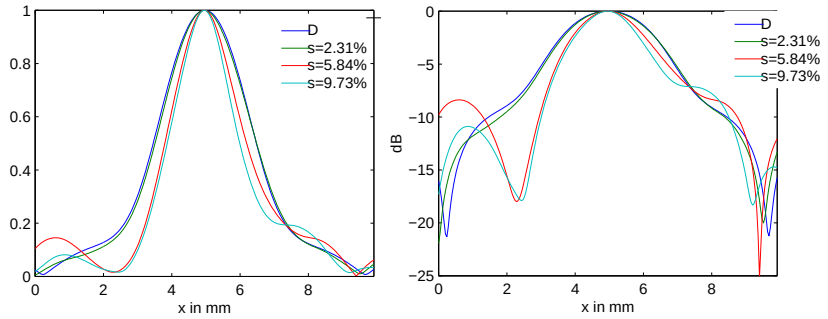

Figure 18: The norm of the back-propagated field at the source level : normalized scale on the left and in dB on the right. Four different curves are drawn in each figure, corresponding to the deterministic (D) and the three random media ($s = 2.31\%$, $s = 5.84\%$ and $s = 9.73\%$).

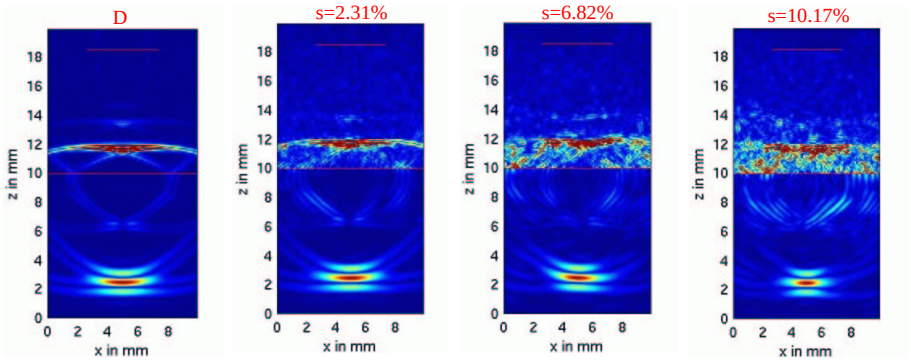

Figure 19: Normalized snapshots of the norm of the velocity. The simulation for the deterministic medium on the left and for the random media on the right. The standard deviation of the fluctuations is 0.0%, 2.31%, 6.82% and 10.17% from left to right. The correlation length is shorter than the wavelength.

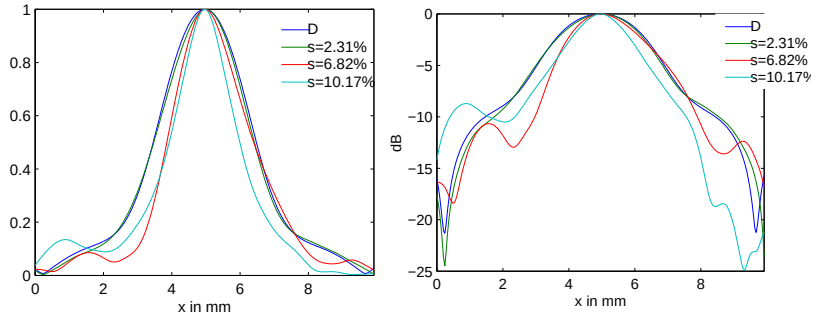

Figure 20: The amplitude of the back-propagated field at the source location : normalized scale on the left and in dB on the right. Four different curves are drawn in each figure, corresponding to the deterministic (D) and the three random media ($s = 2.31\%$, $s = 6.82\%$ and $s = 10.17\%$).

from the source position. Moreover, from the theoretical analysis of time-reversal (Blomgren et al., 2002; Papanicolaou et al., 2002b) we know that the field is statistical stable in the vicinity of the initial source position and thus variations are expected far from the focal spot. We calculate the refocusing resolution (d_{num}) as before by a least squares fit of the curvature at the peak amplitude (in the cross-range direction). The results are given in Table 4, where in the last column we compute the enhancement in the refocusing resolution in the random medium by comparing it to that obtained in the deterministic case. This is the super-resolution effect caused by multipathing. For acoustic waves the **effective** cross-range resolution is $d_e = \lambda L/\alpha_e$ and so the **effective** size of the TRM α_e is larger, often considerably larger, than its physical size α.

It is important to emphasize that super-resolution is a time domain phenomenon in the sense that refocusing by time reversal in a random medium fluctuates wildly from realization to realization when the initial pulse is narrow band (nearly time harmonic). It is only in the time domain (broad band) that the refocused signal is statistically stable, or self-averaging, so that super-resolution is not influenced by the different realizations of the underlying random medium. This phenomenon, which is central to understanding the role of multipathing in time reversal, is analyzed numerically and theoretically in (Blomgren et al., 2002) and with more mathematical details in (Papanicolaou et al., 2002b).

C_l in mm	s	max contrast	d_{num} in mm	improvement %
0.0	0.0	0.0	3.89	-
0.5 mm	2.31%	4.01%	3.54	8.97
0.5 mm	5.84%	10.12%	2.65	31.94
0.5 mm	9.73%	16.86%	2.28	41.46
0.3 mm	2.31%	4.01%	3.40	12.58
0.3 mm	6.82%	11.81%	2.69	30.79
0.3 mm	10.17%	17.62%	2.07	46.79

Table 4: The numerical (d_{num}) estimate of the refocusing resolution for time reversal through random media and comparison with the deterministic case.

The results shown in Table 4 demonstrate quantitatively the super-resolution phenomenon: in media with random heterogeneities the refocusing resolution beats the diffraction limit, which is the refocusing resolution in the homogeneous medium. We see clearly that better resolution is obtained as the standard deviation of the fluctuations in the random media increases. That is because as the contrast in the heterogeneities increases, multipathing becomes more important and makes the effective size of the TRM much larger than its physical size. For instance, the results obtained for the medium with $s = 10.17\%$ correspond to a TRM with an effective size which is approximately double its physical size. Note also that in this case the refocusing resolution obtained is close to the pressure wavelength in the solid (which is 1.8 mm) and thus it can be considered as an optimal result.

The statistical stability of super-resolution in time reversal can be seen nicely in Figures 17 and 19. As the variance of the fluctuations in the sound speed of the liquid increases from left to right, the reflected fields in the liquid, above the interface, look more and more disordered and fragmented while the focusing spot in the solid below gets tighter and tighter! Multipathing, which comes from disorder and randomness, makes wave propagation diffuse and unfocused everywhere except near the source location. There, the time

reversed signal refocuses better, and in a statistically stable manner, because of multipathing.

6 Summary and conclusions

We have reproduced numerically the physical experiments of Draeger, Cassereau and Fink (Draeger et al., 1998), which demonstrate refocusing by time reversal in a liquid-solid interface, with the TRM device in the liquid and the source in the solid. We have examined the refocusing resolution and have related it to the propagation distance, the size of the TRM and the wavelength with a simple generalization of the usual formula in acoustics.

We have also examined numerically the statistical stability and super-resolution of refocusing in a random medium. Only the liquid has random fluctuations in the sound speed in our computations, but it is not difficult to do them also when the solid has random inhomogeneities. We see clearly both the statistical stability, for broad band signals, and super-resolution because of multipathing. The theoretical analysis of these phenomena is presented in (Blomgren et al., 2002) and, in a more mathematical way, in (Papanicolaou et al., 2002b) for acoustic waves in the paraxial approximation. The extension of the theory to the present context is not simple because we may have to use the full radiative transport theory of (Ryzhik et al., 1996), along with various additional approximations.

The importance of statistical stability is explored further in (Borcea et al., 2002) where we show how time reversal can be used for **imaging** in random media, with acoustic waves. The extension of this imaging methodology to the liquid-solid interface case, in the presence of random inhomogeneities, is of great interest in many applications in non-destructive testing, mine detection and elsewhere.

References

Bécache, E., Joly, P., and Tsogka, C. (1997). Eléments finis mixtes et condensation de masse en élastodynamique linéaire. (i) construction. *C.R. Acad. Sci. Paris*, t. 325, Série I:545–550.

Bécache, E., Joly, P., and Tsogka, C. (to appear). Fictitious domains, mixed finite elements and perfectly matched layers for 2d elastic wave propagation. *J. Comp. Acous.*

Bérenger, J. (1994). A perfectly matched layer for the absorption of electromagnetic waves. *Journal of Comp. Physics.*, **114**:185–200.

Blomgren, P., Papanicolaou, G., and Zhao, H. (2002). Super-resolution in time-reversal acoustics. *J. Acoust. Soc. Am.*, 111:238–248.

Borcea, L., Papanicolaou, G., Tsogka, C., and Berryman, J. (2002). Imaging and time reversal in noisy environments. *Inverse Problems*, 18:1247–1279.

Collino, F. and Tsogka, C. (2001). Application of the pml absorbing layer model to the linear elastodynamic problem in anisotropic heteregeneous media. *Geophysics*, 66(1):294–305.

Derode, A., Roux, P., and Fink, M. (1995). Robust Acoustic Time Reversal with High-Order Multiple Scattering. *Physical Review Letters*, 75(23):4206–4209.

Dowling, D. R. and Jackson, D. R. (1990). Phase Conjugation in Underwater Acoustics. *Journal of the Acoustical Society of America*, 89:171–181.

Dowling, D. R. and Jackson, D. R. (1992). Narrow-band Performance of Phase-conjugate Arrays in Dynamic Random Media. *Journal of the Acoustical Society of America*, 91:3257–3277.

Draeger, C., Cassereau, D., and Fink, M. (1997). Theory of time-reversal process in solids. *J. Acoust. Soc. Am*, 102(3):1289–1295.

Draeger, C., Cassereau, D., and Fink, M. (1998). Acoustic time reversal with mode conversion at a solid-flui interface. *Applied Physics Letters*, 72(13):1567–1569.

Fink, M. (1999). Time-Reversed Acoustics. *Scientific American*, pages 91–97.

Kuperman, W. A., Hodgkiss, W. S., Song, H. C., Akal, T., Ferla, C., and Jackson, D. R. (1997). Phase Conjugation in the Ocean: Experimental Demonstration of an Acoustic Time-Reversal Mirror. *Journal of the Acoustical Society of America*, 103(1):25–40.

Papanicolaou, G., Ryzhik, L., and Solna, K. (2002a). Statistical stability in time reversal. *Submitted to SIAM J. on Applied Mathematics*.

Papanicolaou, G. C., Ryzhik, L., and Solna, K. (2002b). The parabolic approximation and time reversal in a random medium. *to appear in Matematica Contemporanea*.

Ryzhik, L. V., Papanicolaou, G. C., and Keller, J. B. (1996). Transport Equations for Elastic and Other Waves in Random Media. *Wave Motion*, 24:327–370.